Chin. Phys. Lett. **39**, 077101 (2022)

Competition of Quantum Anomalous Hall States and Charge Density Wave in a Correlated Topological Model

Xin Gao(高鑫)[1], Jian Sun(孙健)[1], Xiangang Wan(万贤纲)[2,3], and Gang Li(李刚)[1,4*]

[1]*School of Physical Science and Technology, ShanghaiTech University, Shanghai 201210, China*
[2]*National Laboratory of Solid State Microstructures and School of Physics, Nanjing University, Nanjing 210093, China*
[3]*Collaborative Innovation Center of Advanced Microstructures, Nanjing University, Nanjing 210093, China*
[4]*ShanghaiTech Laboratory for Topological Physics, ShanghaiTech University, Shanghai 201210, China*

(Received 12 April 2022; accepted manuscript online 31 May 2022)

We investigate the topological phase transition driven by non-local electronic correlations in a realistic quantum anomalous Hall model consisting of d_{xy}–$d_{x^2-y^2}$ orbitals. Three topologically distinct phases defined in the non-interacting limit evolve to different charge density wave phases under correlations. Two conspicuous conclusions were obtained: The topological phase transition does not involve gap-closing and the dynamical fluctuations significantly suppress the charge order favored by the next nearest neighbor interaction. Our study sheds light on the stability of topological phase under electronic correlations, and we demonstrate a positive role played by dynamical fluctuations that is distinct to all previous studies on correlated topological states.

DOI: 10.1088/0256-307X/39/7/077101

Since the discovery of the quantum Hall effect and the understanding of quantized conductivity in terms of Thouless–Kohomoto–Nightingale–Nijs (TKNN) number,[1–3] the study of unconventional topological systems has become one of the central topics in modern condensed matter physics. Haldane pioneered in the fundamental understanding of time-reversal (TR) symmetry breaking and quantum anomalous Hall (QAH) states.[4]

The artificial complex hopping in the Haldane model can be understood as a higher-order perturbation down-folded from the spin-orbit coupling (SOC) term in a multiorbital model. Thus, the most economical realization of the Haldane model in a realistic material system would be a two-orbital model with SOC on a honeycomb lattice. The most straightforward choice fulfilling such a condition is the spin-polarized orbitals, in which $l_z s_z$ provides the onsite SOC between the two orbitals. Such a mechanism has been realized in the TR symmetric monolayer bismuthene on the SiC(0001) substrate and experimentally confirmed as a large-gap quantum spin Hall system.[5,6]

The same mechanism also applies to the correlated d-orbitals.[7–12] The expectation value of $l_z s_z$ between d_{xy} and $d_{x^2-y^2}$ is intrinsically nonzero, as such a four-band correlated model on honeycomb lattice can be defined. Taking $(|\phi^{\rm A}_{d_{xy}}\rangle, |\phi^{\rm A}_{d_{x^2-y^2}}\rangle, |\phi^{\rm B}_{d_{xy}}\rangle, |\phi^{\rm B}_{d_{x^2-y^2}}\rangle)$ as the basis, we have the simplest tight-binding model for a QAH state on correlated d-orbitals.

$$H_0(k) = \begin{pmatrix} 0 & 2i\lambda & h_{\alpha\alpha}(k) & h_{\alpha\beta}(k) \\ -2i\lambda & 0 & h_{\beta\alpha}(k) & h_{\beta\beta}(k) \\ h^*_{\alpha\alpha}(k) & h^*_{\alpha\beta}(k) & 0 & 2i\lambda \\ h^*_{\beta\alpha}(k) & h^*_{\beta\beta}(k) & -2i\lambda & 0 \end{pmatrix}, \quad (1)$$

where λ is the SOC strength and factor 2 stems from the two overlaps of complex spherical harmonics $Y_2^{\pm 2}$; $h_{\alpha\alpha}$, $h_{\alpha\beta}$, and $h_{\beta\beta}$ are the intra- and inter-orbital hoppings with more details explained in the Supplementary Information.

Equation (1) is a spinless model describing a system fully spin-polarized with only one spin component controlling the low-energy excitations. This four-band QAH model contains three topologically different phases with Chern number $C = -1, 0, 2$. The phase transition between any two phases occurs when the valence and conduction bands cross to close the bandgap. Due to the lack of the other spin, only the local SOC contributes. Furthermore, as d_{xy} and $d_{x^2-y^2}$ favor a nonzero local SOC $\langle d_{xy}|l_z s_z|\phi_{d^{x^2-y^2}}\rangle$ that is usually the largest one among all the SOC terms, this model features a large-gap QAH state that may be utilized in high-temperature spintronic device applications. Furthermore, this model corresponds precisely to the low-energy excitations of a large class of iron halogenides, represented by $FeBr_3$.[9]

*Corresponding author. Email: ligang@shanghaitech.edu.cn
© 2022 Chinese Physical Society and IOP Publishing Ltd

Correlated Tight-Binding Model of QAH. The reduced dimensionality and the correlated d-orbital imply that the QAH phases of Eq. (1) are subject to strong electronic correlations. The stability of the topological phase against correlations has been studied in the context of the Kane–Mele–Hubbard model[13–33] or the spinful Bernevig–Hughes–Zhang model,[34–39] where the non-interacting limit of the model is a topologically trivial semimetal. Distinct from these studies, our multi-orbital model already displays three topologically distinct phases in the non-interacting limit. Thus, there is no need for our model to require complex hopping, and the electronic correlations directly interact with the topological phases.

To study the robustness of the QAH states against electronic correlations, here we consider the nonlocal Coulomb repulsions.

$$H_{\text{int}} = V_1 \sum_{\langle i,j\rangle} n_i n_j + V_2 \sum_{\langle\langle i,j\rangle\rangle} n_i n_j. \tag{2}$$

V_1 is the density-density interaction between the nearest-neighbor sites, which couples electrons at different sublattices. For simplicity, we assume the same interaction strength for both inter-orbital and intra-orbital correlations, and the electron occupancy is half-filling. Here $n_i = \sum_\alpha n_{i\alpha}$ is the total occupancy at site i. V_2 is same as V_1, but for the next nearest-neighbor interaction which couples the same sublattice. In order to compare with the spinless Haldane–Hubbard model on the same basis, we have neglected the inter-orbital local interactions and focus only on the nonlocal interactions favoring charge density wave (CDW) formation. The inclusion of the local inter-orbital repulsion favors the charge redistribution between the two orbitals, leading to a possible orbital order that we will not consider in our work.

Without dedicated calculations, let us first try to intuitively understand what V_1 and V_2 do on the model. For any positive value of V_1, electrons experience a repulsion when both nearest-neighbor sites are occupied, e.g., $\langle n_{\text{A}}\rangle = \langle n_{\text{B}}\rangle = 0.5$. Electrons tend to distribute unevenly within each dimmer to minimize the potential energy associated with V_1. As V_1 would increase the potential energy, at half-filling, the most economical way to distribute electrons is to occupy both orbitals on one sublattice and let the other sublattice empty, e.g., $\langle n_{\text{A}}\rangle = 1, \langle n_{\text{B}}\rangle = 0$. The tendency of one sublattice is fully occupied while the other is empty leads to a periodic modulation of the electron density. As a result, a CDW with the same periodicity of the primitive unit cell will develop as shown in Fig. 1(b).

As for V_2, the situation becomes slightly different. We will obtain another CDW with a larger periodicity $\sqrt{3}\times\sqrt{3}$. V_2 connects the same sublattice forming two decoupled triangular lattices. Triangular lattice is geometrically frustrated that cannot accommodate the same CDW in Fig. 1(b). The smallest CDW pattern compatible with a triangular lattice will have to allow three different electron occupancies in each triangle with classic values $\langle n_1^{\text{A/B}}\rangle = 2$, $\langle n_2^{\text{A/B}}\rangle = 1$, $\langle n_3^{\text{A/B}}\rangle = 0$, see Fig. 1(c). The three different circles with identical colors belong to the same sublattice representing three different electron densities forming a $\sqrt{3}\times\sqrt{3}$ CDW. With only V_2, the $\sqrt{3}\times\sqrt{3}$ CDW on one sublattice is independent of that on the other sublattice. However, with two independent triangular sublattices, another degenerate configuration emerges, i.e. $\langle n_1^{\text{A}}\rangle = 2$, $\langle n_2^{\text{A}}\rangle = 2$, $\langle n_3^{\text{A}}\rangle = 0$, $\langle n_1^{\text{B}}\rangle = 2$, $\langle n_2^{\text{B}}\rangle = 0$, $\langle n_3^{\text{B}}\rangle = 0$. By using the occupation number $n_{\text{A}_1} n_{\text{A}_2} n_{\text{A}_3} n_{\text{B}_1} n_{\text{B}_2} n_{\text{B}_3}$ to label different CDW patterns, in the following section, we will simply denote the three different CDW patterns by V_1 and V_2 as 222000, 220200, and 210210, respectively.

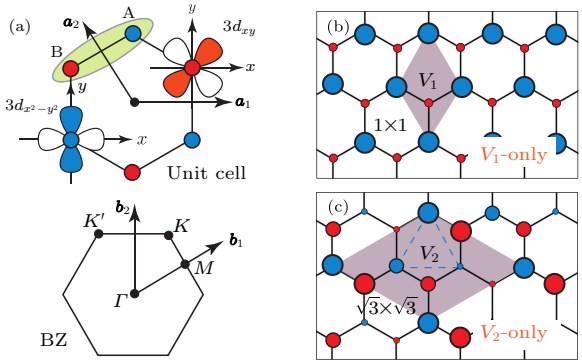

Fig. 1. Tight-binding model and different CDW patterns. (a) The d_{xy}–$d_{x^2-y^2}$ model on honeycomb lattice and the corresponding BZ. (b) Sketch of the CDW mode favored by V_1 where electrons on the two triangular sublattices distribute unevenly. Blue and red colors correspond to the two sublattices, and the size of circles denotes the charge density. (c) The CDW mode favored by V_2 has a larger periodicity as compared to that in (b), as indicated by the light purple area. The classical configuration of this $\sqrt{3}\times\sqrt{3}$ CDW can be either 210210 or 220200, see the main text for more details.

When V_1 and V_2 are simultaneously present, the two CDWs are, unfortunately, not compatible. Residing 210210 on honeycomb lattice will unavoidably have two neighboring sites with high electron densities. Thus, $\sqrt{3}\times\sqrt{3}$ CDW-210210 favored by V_2 competes with the 1×1 CDW-222000 favored by V_1 on honeycomb lattice. They both compete with the nontrivial topology of the four-band QAH model of Eq. (1). It is highly interesting to know the stability of the QAH phase and the way nonlocal charge correlations destroy it.

Results—Static Mean-Field Solution. To understand this problem, we first apply the simple mean-field theory by decoupling the change density of the two sublattices:

$$\hat{n}_{\mathrm{A}_i}\hat{n}_{\mathrm{B}_j} \approx \langle n_{\mathrm{A}_i}\rangle\hat{n}_{\mathrm{B}_j} + \hat{n}_{\mathrm{A}_i}\langle n_{\mathrm{B}_j}\rangle - \langle n_{\mathrm{A}_i}\rangle\langle n_{\mathrm{B}_j}\rangle, \quad (3a)$$

$$\hat{n}_{\mathrm{A}_i}\hat{n}_{\mathrm{A}_j} \approx \langle n_{\mathrm{A}_i}\rangle\hat{n}_{\mathrm{A}_j} + \hat{n}_{\mathrm{A}_i}\langle n_{\mathrm{A}_j}\rangle - \langle n_{\mathrm{A}_i}\rangle\langle n_{\mathrm{A}_j}\rangle. \quad (3b)$$

One then arrives at an effective single-particle problem defined by a 12×12 Hamiltonian with $\langle n_{\mathrm{A}_i}\rangle$ and $\langle n_{\mathrm{B}_j}\rangle$ as parameters. After diagonalizing the Hamiltonian and recalculating the charge density from the single-particle eigenstates, one closes the self-consistency loop. At convergence, the different solutions of n_{A_i} and n_{B_j} will identify the ground state. In this work, we have tempts with four different configurations as initial trivial states, i.e., 111111, 210210, 222000, 220200, and stabilize them through the self-consistent mean-field calculations. We then compare their free energies to determine the ground state whenever we can stabilize multiple charge configurations.

We present the mean-field phase diagram in Fig. 2. Figures 2(a)–2(c) show the topological phase diagram of the d_{xy}–$d_{x^2-y^2}$ model under different strengths of V_1 and V_2. When both V_1 and V_2 are absent, the tight-binding model Eq. (2) shows three distinct phases with Chern numbers $C=-1$, $C=0$, and $C=2$. For most values of a/λ and b/λ, the model Eq. (2) is in certain topological nontrivial phase. Only when $a\approx -b$, the model Eq. (1) becomes trivial. As shown in Fig. 2(b), by including interactions, CDW phase emerges in the center of the phase diagram, i.e., $a=b=0$, and gradually expands to larger values of a/λ and b/λ, which is a natural consequence of the competition between kinetic and potential energy.

Through the direct calculation of Chern number, we further confirm that, once CDW appears, the Chern number becomes zero. This new $C=0$ phase, shown by yellow in Figs. 2(a)–2(c), is distinct from the original $C=0$ phase colored in blue along the off-diagonal of the phase diagram. The latter is an ordinary band insulator, while the new one is a CDW insulator with charge pattern 222000. The emergence of the CDW-222000 in Fig. 2 breaks all three band insulating phases, redistributing charge from equal density, i.e., 111111 pattern, to 222000.

As indicated by the comparison of Figs. 2(b) and 2(c), finite V_2 significantly shrinks the CDW-222000 size, confirming that V_2 competes with V_1. Consequently, V_2 stabilizes topological nontrivial phase and allow them to persist to larger values of V_1. Individually, both V_1 and V_2 destabilize the topological phases. However, when they coexist, their competition stabilizes the topological phases because they tend to destroy the CDW pattern favored by each other.

Figures 2(d) and 2(e) display the V_1–V_2 phase diagram with three characteristic model parameter sets of a/λ, b/λ. We choose $a/\lambda=3.5$, $b/\lambda=-3.5$ for $C=0$ phase, $a/\lambda=1.0$, $b/\lambda=-6.0$ for $C=-1$ phase, and $a/\lambda=3.2$, $b/\lambda=2.6$ for $C=2$ phase. Both interacting phase diagrams in Figs. 2(d) and 2(e) contain two types of CDW states, i.e., CDW-222000 phase for larger V_1 and smaller V_2, and CDW-210210 state for larger V_2. In between, no charge modulation is found, where the model keeps its topological nature characterized by the tight-binding model, but with a modified dispersion. It is clear that the presence of next nearest-neighbor interaction V_2 suppresses the sublattice CDW-222000. Critical value of V_1 becomes larger with the increase of V_2. However, CDW-222000 is more robust than other types of CDW when V_1 is sufficiently large. CDW-222000 always wins the competition with other types of CDW favored by V_2. In our calculations, we did not find pure CDW-220200 phase and it is degenerate with CDW-210210 at larger V_1. However, for smaller V_1, CDW-210210 is always more stable than 220200.

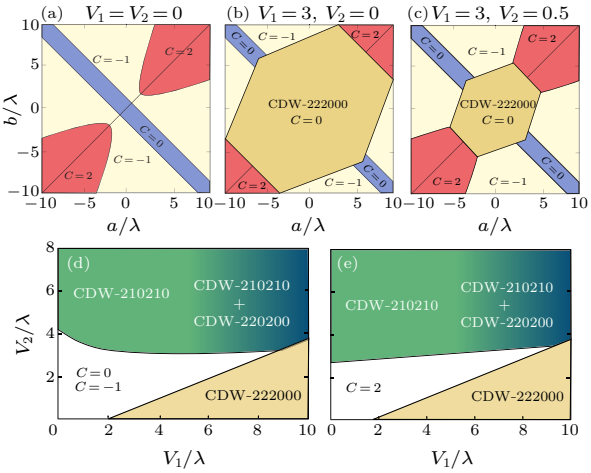

Fig. 2. Mean-field phase diagram of the d_{xy}–$d_{x^2-y^2}$ model under different interactions, i.e., phase diagrams as functions of a/λ and b/λ at (a) $V_1=V_2=0$, (b) at $V_1=3.0$, $V_2=0.0$, (c) at $V_1=3.0$, $V_2=0.5$. [(d), (e)] The phase diagrams as functions of V_1/λ and V_2/λ for the fixed tight-binding model parameters a/λ and b/λ. $C=0$ and $C=-1$ phases have very similar dependences on V_1/λ and V_2/λ, and they are shown in (d). (e) Phase diagram for $C=2$ phase.

Dynamical Fluctuations. After understanding the static mean-field phase diagram, we further study the dynamical fluctuation effect on the QAH phase. Despite of the much richer phase diagram predicted by static mean-field calculations, most of the mean-filed predictions beyond the density decoupling are known

to be unstable.[16–21,23–31,40,41] In particular, topological Mott phase emerging from the complex hopping is completely suppressed by dynamical fluctuations. Thus, beyond the static mean-field study shown before, we want to know if the topological phases of our model survive under a more sophisticated consideration of correlation effect. We would emphasize that out study is distinct to the previous studies,[16–20,23–31] which started with a topological trivial state and expected to trigger topological phase by electronic correlations. The nontrivial topology builds in our tight-binding model. No complex decoupling, which is usually unstable under dynamical fluctuations, is crucially needed in our construction. Thus, we expect a more robust topological phase in this realistic model.

To this end, we use exact diagonalization (ED) to solve Eqs. (1) and (2) in three different strategies. We firstly use ED as an impurity solver in a dynamical mean-field theory (DMFT) calculation with only local charge fluctuations. Secondly, going beyond DMFT to partially account for nonlocal charge fluctuations, we further solve a cellular-DMFT (C-DMFT) equation with six-site unit cell. In the third strategy, a six-site cluster with periodic boundary condition is solved directly by ED. The three numerical calculations, i.e., DMFT, C-DMFT, and ED, are complementary in nature so that we can understand the influence of non-local charge fluctuations and boundary effect from their comparison. Comparing C-DMFT to DMFT, one gets insight of the non-local effect. Comparing C-DMFT to ED with the same cluster size, one can understand the boundary effect. See the Supplementary Information for more details.

Figure 3 displays the corresponding results at $V_2 = 0$. For a better comparison, we also show the static mean-field results in Fig. 3(a). Figures 3(b)–3(d) contain dynamical fluctuations beyond the static mean-field solution. As shown in Fig. 3(b), dynamical fluctuations included in the DMFT significantly enlarge the critical values V_{1c} by suppressing the CDW-222000 phase. At the same time, the difference among V_{1c} for the three phases also becomes more pronounced as compared to Fig. 3(a). The DMFT impurity contains only two sites and they are coupled by V_1. Embedding such a small size system into lattice artificially overemphasizes the Coulomb repulsion between neighboring sites. As clearly indicated by Fig. 3(c), the nonlocal spatial fluctuations contained in a six-site C-DMFT calculations render a smaller V_{1c} than those in DMFT, but larger than those obtained in static mean-field calculations. C-DMFT is a better approximation than both DMFT and static mean-field that it contains both dynamical and some spatial fluctuations, thus, V_{1c} obtained in C-DMFT is supposed to be a more reliable value. ED, on the other hand, suffers a finite cluster issue, thus boundary effect in ED is worse than C-DMFT. From Fig. 3, we conclude that dynamical fluctuations push phase boundary of CDW-222000 to a larger value of V_1, further stabilizing the topological phase.

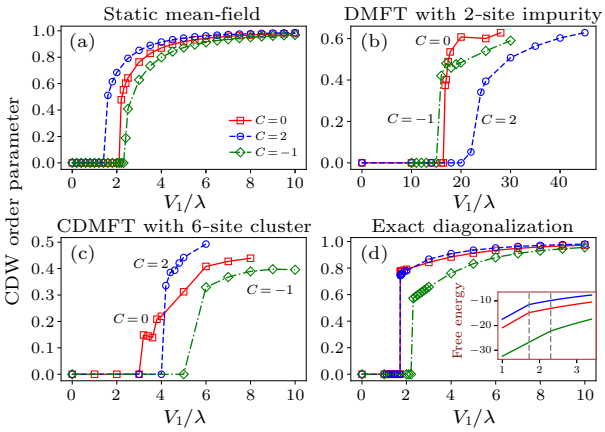

Fig. 3. CDW order parameters versus nearest-neighbor Coulomb repulsion V_1, i.e., results from (a) mean-field solution, (b) DMFT with 2-site impurity, (c) C-DMFT with 6-site cluster calculations, and (d) exact diagonalization. The inset shows the free energy evolution around the transition boundary, indicating their first-order nature. The same colors as the main plot in (d) are used.

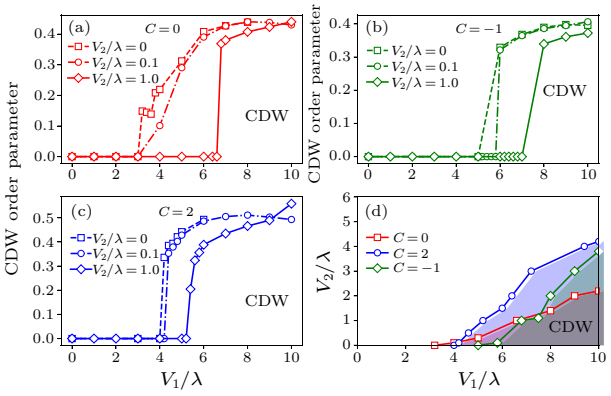

Fig. 4. V_1–V_2 phase diagram. (a)–(c) The $C = 0$, -1, and 2 phases boundaries to CDW for three different V_2/λ. Increasing V_2/λ clearly suppresses the CDW-222000 state (indicated as CDW), pushing V_{1c} to larger values. (d) The V_1–V_2 phase diagram from C-DMFT.

As shown in Fig. 4, including V_2 the topological phases are further stabilized. In Figs. 4(a)–4(c), we show the critical V_{1c} of the three different phases for different values of V_2. Increasing V_2 clearly shifts the CDW phase boundary to the right, which is consistent with the mean-field prediction discussed in Figs. 2(d) and 2(e), However, the CDW-210210 and CDW-220200 phases contained in the mean-field phase diagrams in Figs. 2(d) and 2(e) completely dis-

appear upon the inclusion of the dynamical fluctuations, in sharp contrast to CDW-222000 phase. The latter is only slightly suppressed by V_2. We confirmed that, at least up to $V_2/\lambda = 20$, CDW-210210 and CDW-220200 phases cannot be stabilized, which is further supported by the ED calculation on the isolated six-site cluster. In ED, there is no indication of the CDW-210210 and CDW-220200 for any value of V_2. Furthermore, the CDW-222000 phase is also completely suppressed down to $V_2 = 0$ line. Any finite V_2 will immediately kill the CDW-222000 phase, which is likely due to the boundary condition and the finite-size effect in ED. Nevertheless, both ED and C-DMFT with six-site cluster calculations consistently show the breakdown of CDW (210210, 220200) favored by the next nearest-neighbor repulsion V_2. Only the CDW-222000 emerging from the nearest-neighbor interaction V_1 survives, whose phase space, however, significantly shrinks as compared to the mean-field prediction.

Discussions and Conclusions. Two conspicuous consequences of the interaction effect deserve further explication. First, from the inspection of the local density of state, we find that the phase transition from QAH to CDW does not experience a gap-closing process even in the static mean-field level. In the inset of Fig. 3(d) we show the free energy from exact diagonalization. The free energy in the non-CDW (CDW) phase at a smaller (larger) V_1 regime intersects at the transition boundary with a clear slope change, indicating a first-order phase transition. This is consistent with some previous works.[38,42–44] The QAH and the CDW phases differ in the sublattice/translational symmetry. Thus, there is no need for such a topological phase transition to close the gap. In this sense, it is similar to a recently discovered topological phase transition in the twisted transition metal dichalcogenide (TMD),[45] where a correlated insulating phase becomes a QAH insulator without closing the gap. Phenomenologically, the two phase transitions are both between a topologically trivial insulator and a QAH state. Yet, the nature of the correlated insulating phase in twisted TMD is not known and was anticipated as a non-magnetic Mott insulator or a 120-degree antiferromagnetic insulator, while the QAH phase is possibly valley polarized. Our work thus sheds new light and provides additional insights to this timely topic. According to our calculations, a CDW insulator may also be a good candidate to the correlated insulating phase observed in twisted TMD.

We note that, due to the presence of three topologically distinct phases in the model, we are able to examine their responses to charge modulation on equal footing. We find that both the band-insulator with $C = 0$ and the Chern insulator with $C = -1, 2$ transform to the CDW insulating states by the first-order transition. In this sense, there is no difference between topologically trivial and nontrivial phases under the electronic correlations. The CDW phase appears when the self-energy of A, B sublattices starts to deviate. Otherwise, the correlation effect mainly rigidly shifts the dispersion. Second, the breakdown of the CDW-210210 + CDW-220200 is astonishing. Their destruction is distinct to that of the topological Mott phase studied in the Kane–Mele–Hubbard model,[31] where the latter requires an unusual decomposition of V_2. However, CDW-210210 + CDW-220200 is a density modulation and is believed to be much more stable. In our calculations, the loss of longer-range CDW is unlikely attributed to the finite-cluster size effect, as smaller systems tend to overestimate non-local order.

In summary, we have studied the quantum phase transition in a correlated topological model. This model is a two-orbital extension of the Haldane model, and the $C = -1$ phase was realized in the monolayer of $FeBr_3$ family. All three phases, i.e., $C = 0$, $C = -1$, and $C = 2$, were examined against the non-local Coulomb interaction. We found that the QAH phase is stable till the intermediate value of interactions. The destruction of the QAH phase and the emergence of the CDW phase are simultaneous. With the dynamical fluctuations, we find the CDW solution from the static mean-field becomes less stable at a smaller interaction regime, resulting in an enhanced QAH phase. The QAH phase expands in the parameter space due to the destruction of the CDW phase by the dynamical fluctuations. At the same time, the CDW favored by the next nearest-neighbor interaction V_2 becomes unstable under dynamical fluctuations. No emergent topological phase triggered by electronic correlations is found.

Our calculations consistently show that the non-local electronic repulsion induces a phase transition to the topological trivial CDW phase. The transition does not accompany gap-closing, unlike the topological insulator to band insulator transition. Our work sheds light on the interacting topological phases. We point out that the density-density interaction and the normal self-energy disfavor the topological phase. Thus, the search for an interaction-triggered topological phase requires new types of interactions and anomalous self-energy to come into play.

Acknowledgement. This work was supported by the National Natural Science Foundation of China

(Grant No. 11874263), the National Key R&D Program of China (Grant No. 2017YFE0131300), and Shanghai Technology Innovation Action Plan (2020-Integrated Circuit Technology Support Program 20DZ1100605, 2021-Fundamental Research Area 21JC1404700). Part of the calculations was performed at the HPC Platform of ShanghaiTech University Library and Information Services and at the School of Physical Science and Technology, ShanghaiTech University.

References

[1] Klitzing K V, Dorda G and Pepper M 1980 *Phys. Rev. Lett.* **45** 494
[2] Thouless D J, Kohmoto M, Nightingale M P and den Nijs M 1982 *Phys. Rev. Lett.* **49** 405
[3] Nayak C, Simon S H, Stern A, Freedman M and Sarma S D 2008 *Rev. Mod. Phys.* **80** 1083
[4] Haldane F D M 1988 *Phys. Rev. Lett.* **61** 2015
[5] Reis F, Li G, Dudy L, Bauernfeind M, Glass S, Hanke W, Thomale R, Schäfer J and Claessen R 2017 *Science* **357** 287
[6] Li G, Hanke W, Hankiewicz E M, Reis F, Schäfer J, Claessen R, Wu C and Thomale R 2018 *Phys. Rev. B* **98** 165146
[7] Rüegg A and Fiete G A 2011 *Phys. Rev. B* **84** 201103
[8] Yang K Y, Zhu W, Xiao D, Okamoto S, Wang Z and Ran Y 2011 *Phys. Rev. B* **84** 201104
[9] Sui Q, Zhang J, Jin S, Xia Y and Li G 2020 *Chin. Phys. Lett.* **37** 097301
[10] Wang H and Wang J 2021 *Phys. Rev. B* **103** L081109
[11] Li Z, Han Y and Qiao Z 2021 *Phys. Rev. B* **104** 205401
[12] Li J, Yao Q, Wu L, Hu Z, Gao B, Wan X and Liu Q 2022 *Nat. Commun.* **13** 919
[13] Rachel S and Le H K 2010 *Phys. Rev. B* **82** 075106
[14] Zheng D, Zhang G M and Wu C 2011 *Phys. Rev. B* **84** 205121
[15] Budich J C, Thomale R, Li G, Laubach M and Zhang S C 2012 *Phys. Rev. B* **86** 201407
[16] Grushin A G, Castro E V, Cortijo A, de Juan F, Vozmediano M A H and Valenzuela B 2013 *Phys. Rev. B* **87** 085136
[17] García-Martínez N A, Grushin A G, Neupert T, Valenzuela B and Castro E V 2013 *Phys. Rev. B* **88** 245123
[18] Daghofer M and Hohenadler M 2014 *Phys. Rev. B* **89** 035103
[19] Capponi S and Läuchli A M 2015 *Phys. Rev. B* **92** 085146
[20] Motruk J, Grushin A G, de Juan F and Pollmann F 2015 *Phys. Rev. B* **92** 085147
[21] Hohenadler M, Lang T C and Assaad F F 2011 *Phys. Rev. Lett.* **106** 100403
[22] Yu S L, Xie X C and Li J X 2011 *Phys. Rev. Lett.* **107** 010401
[23] Castro E V, Grushin A G, Valenzuela B, Vozmediano M A H, Cortijo A and de Juan F 2011 *Phys. Rev. Lett.* **107** 106402
[24] Sorella S, Otsuka Y and Yunoki S 2012 *Sci. Rep.* **2** 992
[25] Kurita M, Yamaji Y and Imada M 2016 *Phys. Rev. B* **94** 125131
[26] Scherer D D, Scherer M M and Honerkamp C 2015 *Phys. Rev. B* **92** 155137
[27] Volpez Y, Scherer D D and Scherer M M 2016 *Phys. Rev. B* **94** 165107
[28] Kaneko R, Tocchio L F, Valentí R and Gros C 2016 *Phys. Rev. B* **94** 195111
[29] de la Peña D S, Lichtenstein J and Honerkamp C 2017 *Phys. Rev. B* **95** 085143
[30] Bijelic M, Kaneko R, Gros C and Valentí R 2018 *Phys. Rev. B* **97** 125142
[31] Raghu S, Qi X L, Honerkamp C and Zhang S C 2008 *Phys. Rev. Lett.* **100** 156401
[32] Shao C, Castro E V, Hu S and Mondaini R 2021 *Phys. Rev. B* **103** 035125
[33] Yi T C, Hu S, Castro E V and Mondaini R 2021 *Phys. Rev. B* **104** 195117
[34] Bernevig A B, Hughes T L and Zhang S C 2006 *Science* **314** 1757
[35] Budich J C, Trauzettel B and Sangiovanni G 2013 *Phys. Rev. B* **87** 235104
[36] Wang L, Dai X and Xie X C 2012 *Europhys. Lett.* **98** 57001
[37] Li G, Hanke W, Sangiovanni G and Trauzettel B 2015 *Phys. Rev. B* **92** 235149
[38] Amaricci A, Budich J C, Capone M, Trauzettel B and Sangiovanni G 2015 *Phys. Rev. Lett.* **114** 185701
[39] Wu H Q, He Y Y, Fang C, Meng Z Y and Lu Z Y 2016 *Phys. Rev. Lett.* **117** 066403
[40] Griset C and Xu C 2012 *Phys. Rev. B* **85** 045123
[41] Laubach M, Reuther J, Thomale R and Rachel S 2014 *Phys. Rev. B* **90** 165136
[42] Ezawa M, Tanaka Y and Nagaosa N 2013 *Sci. Rep.* **3** 2790
[43] Varney C N, Sun K, Rigol M and Galitski V 2010 *Phys. Rev. B* **82** 115125
[44] Barbarino S, Sangiovanni G and Budich J C 2019 *Phys. Rev. B* **99** 075158
[45] Li T, Jiang S, Shen B, Zhang Y, Li L, Tao Z, Devakul T, Watanabe K, Taniguchi T, Fu L, Shan J and Mak K F 2021 *Nature* **600** 641

Supplementary Information

Competition of quantum anomalous Hall states and charge density wave in a correlated topological model

Xin Gao (高鑫),[1] Jian Sun(孙健),[1] Xiangang Wan(万贤纲), [2,3] and Gang Li(李刚)[1,4,†]

[1]*School of Physical Science and Technology, ShanghaiTech University, Shanghai 201210, China*
[2]*National Laboratory of Solid State Microstructures and School of Physics, Nanjing University, Nanjing 210093, China*
[3]*Collaborative Innovation Center of Advanced Microstructures, Nanjing University, Nanjing 210093, China*
[4]*ShanghaiTech Laboratory for Topological Physics, ShanghaiTech University, Shanghai 201210, China*

I. TIGHT-BINDING MODEL

The tight-binding model studied in this work is a two-orbital model defined on a honeycomb lattice. For simplicity, we only include the nearest-neighbor hopping which couples the two sublattices. On the same sublattice, distinct orbitals are orthogonal. It is easy to show that, under symmetry constrain, $h_{\alpha\alpha}(k) = (3a+b)(1+e^{ik_1})/4+be^{-ik_2}$, $h_{\beta\beta}(k) = (a+3b)(1+e^{ik_1})/4+ae^{-ik_2}$, and $h_{\alpha\beta} = \sqrt{3}(a-b)(1-e^{ik_1})/4$. α, β denote d_{xy} and $d_{x^2-y^2}$, respectively. a, b are model parameters, and k_1, k_2 are the momenta in the first Brillouin zone (BZ), i.e. the fractions of reciprocal lattice vectors $\mathbf{b}_1$ and $\mathbf{b}_2$. On the basis of $|\phi^A_{d_{xy}}\rangle, |\phi^A_{d_{x^2-y^2}}\rangle, |\phi^B_{d_{xy}}\rangle, |\phi^B_{d_{x^2-y^2}}\rangle$, the Hamiltonian matrix can be cast as

$$H_0'(k) = \begin{pmatrix} 0 & 0 & h_{\alpha\alpha}(k) & h_{\alpha\beta}(k) \\ 0 & 0 & h_{\beta\alpha}(k) & h_{\beta\beta}(k) \\ h^*_{\alpha\alpha}(k) & h^*_{\alpha\beta}(k) & 0 & 0 \\ h^*_{\beta\alpha}(k) & h^*_{\beta\beta}(k) & 0 & 0 \end{pmatrix}. \tag{1}$$

As atomic orbitals are orthogonal in the same sublattice, the first and the last 2×2 Hamiltonian blocks are zero. Only the hopping between A-B sublattice contributes. Let us further consider the SOC, it contains both local and nonlocal contributions with the former being the largest term. We neglect the nonlocal SOC, which does not qualitatively affect our model. Atomic SOC between d_{xy} and $d_{x^2-y^2}$ orbitals is a constant. Without it, two eigenvalues of $H_0(k)$ degenerate at K-point at the Fermi level. After including the SOC term, the following Hamiltonian is obtained and a topological gap immediately opens leading to the QAH phase, which is the starting point of our correlated study in this work.

$$H_0(k) = \begin{pmatrix} 0 & 2i\lambda & h_{\alpha\alpha}(k) & h_{\alpha\beta}(k) \\ -2i\lambda & 0 & h_{\beta\alpha}(k) & h_{\beta\beta}(k) \\ h^*_{\alpha\alpha}(k) & h^*_{\alpha\beta}(k) & 0 & 2i\lambda \\ h^*_{\beta\alpha}(k) & h^*_{\beta\beta}(k) & -2i\lambda & 0 \end{pmatrix}. \tag{2}$$

There are three independent parameters a, b, and λ. Depending on the value a/λ and b/λ, there will be three phases with distinct topological numbers, i.e. $c = 0, -1$, and $c = 2$.

The $C = -1$ phase has been shown to correspond exactly to the low-energy excitation of $FeBr_3$ [1]. It is different from Haldane model [2] and Kane-Mele model [3] in the following way: First, our QAH model does not contain any artificial complex hopping term. Instead, a local SOC between the two orbitals triggers the nontrivial topological states of the model. Secondly, our QAH model is a correlated topological model defined for the d_{xy} and $d_{x^2-y^2}$ orbitals, which is a realistic construction for correlated topological systems. Thus, it is interesting to know the effect of electronic correlation on the ground state of this model.

Many previous studies of correlation effect on topological model aim to trigger topological state from Haldane model or Kane-Mele model without the complex hopping term, and expect to generate it from the dynamic evolution. In contrast, we start with a correlated model of intrinsic topology and try to understand its robustness. We characterize the correlated topology by using different approximated methods, as no exact solution is available. We adopt the static mean-field approximation, the dynamical mean-field theory (DMFT), the Cellular DMFT (CDMFT) and exact diagonalization (ED) approaches. These methods are subject to different levels of approximations. By combining them, we expect to reduce numerical bias and obtain a consistent characterization of the correlated topological state. In the following table SI-1, we compare the four approximated approaches in terms of dynamical fluctuations, spatial fluctuations, and thermodynamic limit. A numerically exact method would contain dynamical fluctuation, long-range spatial fluctuations, and is built at thermodynamic limit. By comparing the results from the four approximated methods, we expect to understand the effect of these three features and get insights of the exact solution.

TABLE SI-1. Comparison of the four methods reveals their different levels of approximation.

Method	Dynamical Fluctuations	Spatial Fluctuations	Thermodynamic Limit
Static Mean-Field	No	No	Yes
DMFT	Yes	No	Impurity embedding
CDMFT	Yes	Only short-range	Cluster embedding
ED	Yes	Only short-range	No

A. Chern number

In the tight-binding model and the static mean-field calculations, one obtains the wavefunctions which can be employed to calculate the Chern number from BZ integration. To do this, we follow the recipe of T. Fukui [4] and calculate the Chern number by discretizing BZ into small patches. The Chern number is given by a sum of the winding number of the $U(1)$ gauge transformation along the boundary of a patch. The $U(1)$ link is defined as

$$U_\nu(k_l) \equiv \langle n(k_l)|n(k_l+\hat{\nu})\rangle/\mathcal{N}_\nu(k_l)\ , \tag{3}$$

where ν is a vector denoting direction ν. Along the boundary of a patch, one can define a lattice field strength, whose imaginary part gives rise to the Chern number

$$\tilde{F}_{12}(k_l) \equiv \ln U_1(k_l)U_2(k_l+\hat{1})U_1(k_l+\hat{2})^{-1}U_2(k_l^{-1}) = a + 2\pi i n_{12}(k_l)\ . \tag{4}$$

Here, a is a real number, and the sum of $n_{12}(k_l)$ for all discrete k_l is the Chern number.

$$\text{Chern number} = \sum_l n_{12}(k_l)\ . \tag{5}$$

In our tight-binding and static mean-field calculations, we directly calculate the wave functions and determine the Chern number with 20×20 momentum patches in the first BZ, which is sufficient to get a converged solution. In DMFT, CDMFT, and ED calculations, due to the lack of wave functions and enough momentum resolution, we did not calculate the Chern number.

B. Static mean-field equation

To account for both V_1 and V_2, in the main text, our static mean-field calculations were performed in a six-site unit-cell as shown in Fig. 1**c** of the main text. There are three sites from A-sublattice, and three sites from B-sublattice. d_{xy} and $d_{x^2-y^2}$ orbitals reside at each site. Thus, there are 12 basis functions, which we denote as

$$\{m\}_{1\cdots 12} = \{A_1^{d_{xy}}, A_1^{d_{x^2-y^2}}, A_2^{d_{xy}}, A_2^{d_{x^2-y^2}}, A_3^{d_{xy}}, A_3^{d_{x^2-y^2}}, B_1^{d_{xy}}, B_1^{d_{x^2-y^2}}, B_2^{d_{xy}}, B_2^{d_{x^2-y^2}}, B_3^{d_{xy}}, B_3^{d_{x^2-y^2}}\}\ , \tag{6}$$

Tight-binding model expressed at this basis function is a 12×12 matrix. To transform the interaction part to a quadratic form, we further decompose the density-density interaction by the standard mean-field decoupling

$$\hat{n}_{A_i}\hat{n}_{B_j} \approx \langle n_{A_i}\rangle\hat{n}_{B_j} + \hat{n}_{A_i}\langle n_{B_j}\rangle - \langle n_{A_i}\rangle\langle n_{B_j}\rangle\ , \tag{7a}$$

$$\hat{n}_{A_i}\hat{n}_{A_j} \approx \langle n_{A_i}\rangle\hat{n}_{A_j} + \hat{n}_{A_i}\langle n_{A_j}\rangle - \langle n_{A_i}\rangle\langle n_{A_j}\rangle\ . \tag{7b}$$

The mean-field Hamiltonian is simply obtained by appending each diagonal term of the 12×12 tight-binding matrix with a constant dependent on the charge density of the other sites. This term can be generally written as

$$H_{A_\alpha} = V_1\langle n_B\rangle + 3V_2(\langle n_A\rangle - \langle n_{A_i}\rangle)\ , \tag{8a}$$

$$H_{B_\alpha} = V_1\langle n_A\rangle + 3V_2(\langle n_B\rangle - \langle n_{B_i}\rangle)\ . \tag{8b}$$

$\langle n_{A/B}\rangle = \sum_{i=1}^{3}\sum_{\alpha=d_{xy},d_{x^2-y^2}} n_{A_i/B_i,\alpha}$. As each diagonal term differs slightly depending on the charge densities, diagonalizing the new Hamiltonian matrix yields a new set of dispersions $\epsilon_j(k)$ and eigenstates $|\psi_{j,m}(k)\rangle$, where j denotes the j-th eigenstate, and $m\in[1,12]$ denotes the $m-$th basis component. We proceed to calculate the local density of states $\rho(\epsilon)$ and the new chemical potential μ from

$$\rho(\epsilon) = \frac{1}{N}\sum_{k,j}\delta[\epsilon-\epsilon_j(k)]\ , \int_{-\infty}^{\infty} d\epsilon \frac{\rho(\epsilon)}{\exp[\beta(\epsilon-\mu)+1]} = n_{tot}\ . \tag{9}$$

We fix the particle density to be one per site ($n_{tot} = 6$), corresponding to a half-filling condition, and inverse temperature is taken as $\beta = 1000$. The calculation of new charge density close the mean-field self-consistent loop as

$$\langle n_m \rangle = \frac{1}{N} \sum_k \sum_{j=1}^{12} \frac{|\psi_{j,m}(k)|^2}{\exp[\beta(\epsilon_j(k) - \mu) + 1]} \ . \tag{10}$$

After convergence, we further determine the free energy. Whenever multiple CDW phases are found to be stable in the calculation, we compare their free energy to determine the ground state.

$$\begin{aligned} F = & \frac{1}{N} \sum_k \sum_{j=1}^{12} \frac{\epsilon_k}{\exp[\beta(\epsilon_j(k) - \mu) + 1]} - V_1 \langle n_A \rangle \langle n_B \rangle - 3V_2 (n_{A_1} n_{A_2} + n_{A_1} n_{A_3} + n_{A_2} n_{A_3} + n_{B_1} n_{B_2} + n_{B_1} n_{B_3} + n_{B_2} n_{B_3}) \\ & + k_B T \int d\epsilon \rho(\epsilon) \{ f(\epsilon) \ln[f(\epsilon)] + [1 - f(\epsilon)] \ln[1 - f(\epsilon)] \} \end{aligned} \tag{11}$$

Our self-consistent mean-field calculation starts with a trivial charge density belonging to one of the four states, i.e. 222000, 210210, 220200, and 111111 states. Convergence is achieved if the total difference of the new and old charge density $\Delta = \sum_{m=1}^{12} |\langle n_m^{new} \rangle - \langle n_m^{old} \rangle|$ is smaller than 10^{-5}.

The emergence of the CDW order breaks the symmetry between the two sublattices. Thus, the transition between the QAH phase and the CDW phase does not necessarily close the gap. In the following, we give an intuitive explanation on this point. Following the decomposition of Eq. (7), we update the Hamiltonian Eq. (1) with the correlation effect in the mean-field level and assume there is no orbital order between d_{xy} and $d_{x^2-y^2}$.

$$H^{HF}(k) = \begin{pmatrix} 3V_1 n_B/2 - \mu & 2i\lambda & h_{\alpha\alpha}(k) & h_{\alpha\beta}(k) \\ -2i\lambda & 3V_1 n_B/2 - \mu & h_{\beta\alpha}(k) & h_{\beta\beta}(k) \\ h^*_{\alpha\alpha}(k) & h^*_{\alpha\beta}(k) & 3V_1 n_A/2 - \mu & 2i\lambda \\ h^*_{\beta\alpha}(k) & h^*_{\beta\beta}(k) & -2i\lambda & 3V_1 n_A/2 - \mu \end{pmatrix} . \tag{12}$$

Before the CDW establishes, $n_A = n_B$. The electronic repulsions V_1 only introduce a constant energy term to all bands, which corresponds to a shift of the chemical potential $\mu = 3V_1(n_A + n_B)/2$. Consequently, the charge gap remains the same as the one in the non-interacting limit. When the CDW starts to establish, it creates an energy difference between the A-B sublattice.

$$H^{HF}(k) = \begin{pmatrix} m & 2i\lambda & h_{\alpha\alpha}(k) & h_{\alpha\beta}(k) \\ -2i\lambda & m & h_{\beta\alpha}(k) & h_{\beta\beta}(k) \\ h^*_{\alpha\alpha}(k) & h^*_{\alpha\beta}(k) & -m & 2i\lambda \\ h^*_{\beta\alpha}(k) & h^*_{\beta\beta}(k) & -2i\lambda & -m \end{pmatrix} . \tag{13}$$

Unlike the case of the single-band model where the CDW order parameter always increases the gap, in a multiorbital system, it can either shrink or enlarge the charge gap depending on the amplitude of m, as one will see after diagonalizing Eq. (13). Because m further depends on the charge imbalance of the two sublattices, it is in fact not a free parameter but has to be self-consistently determined. Consequently, the charge gap in a multiorbital model generally does not monotonically change with the increase of the CDW order parameter. Only when m is large enough, does the corresponding free energy become smaller than that of the charge uniform phase, the topological phase transition between the QAH and the CDW occurs with a sudden increase of the CDW order parameter. As shown in Fig.3 of the main text, the first-order phase transition is observed in all calculations. The transition, thus, does not necessarily accompany a gap closure. In Fig. S1, we show the density of states (DOS) from ED calculations on a six-site cluster with periodic boundary conditions. The eight major peaks in each plot correspond to the top and bottom edges of the four bands, thus, the charge gap is easily seen from the peak separation around the Fermi level. In all three topological phase transitions, the charge gap does close and reopen.

II. DYNAMICAL MEAN FIELD THEORY

DMFT is an embedding approach, where a finite-size system called impurity is embedded in the infinite-large lattice. The embedding procedure, on one hand, simplifies the calculations by replacing the problem of solving a lattice Hamiltonian to solving an impurity one. On the other hand, the embedding procedure provides the impurity system a dynamically fluctuating external field, to which the impurity electrons couple. This dynamically fluctuating field is named a hybridization function, which characterizes the coupling between the impurity and the rest of the lattice system. Although the construction of DMFT is conceptually in the thermodynamic limit, the nature of the DMFT approximation respects only the local charge fluctuations.

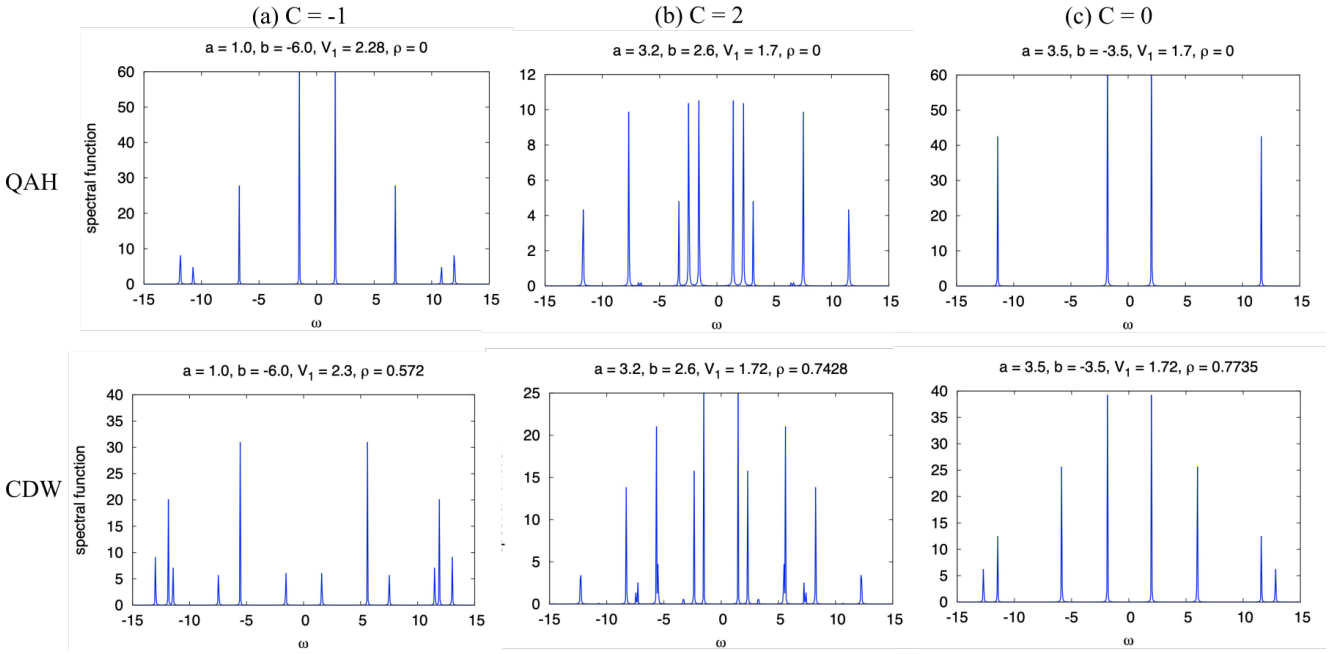

FIG. SI-1. The local DOS before and after the topological phase transition between the QAH and CDW states for all three topological distinct phases. The first row shows the DOS for the QAH phase close to the transition boundary. The second row shows the DOS for the CDW phase slightly after the phase transition. The transition induces an abrupt increase of the CDW order parameter, which is denoted here as ρ. The Fermi level in each plot has been shifted to zero. The charge gap is simply the energy difference between the first two peaks around the Fermi level.

DMFT assumes Green's function of the impurity system to be equal to the local part of the lattice Green's function, which establishes a self-consistent procedure.

$$G^{imp}_{m,n} = \frac{1}{N_k}\sum_k \left[\frac{1}{(i\omega_n+\mu)\mathcal{I} - [H_0(k)] - [\Sigma(i\omega_n)]}\right]_{m,n} , \tag{14}$$

where $\mathcal{I}$ is an unity matrix of the same size of the impurity dimension. In our DMFT study, we take the primitive cell of the honeycomb lattice, which contains two inequivalent sites, as the impurity. $\mathcal{I}$ is then a 4×4 unity matrix. $[H_0(k)]$ is the tight-binding matrix given in Eq. (1), and $[\Sigma(i\omega_n)]$ is the impurity self-energy with the same dimension of the impurity problem. We used ED to solve the impurity problem and obtain $[\Sigma(i\omega_n)]$.

We note that ED works only with Hamiltonians. While, the DMFT embedding procedure spoils the Hamiltonian form of the impurity by introducing the hybridization function, which imposes additional complexity to ED, i.e. the hybridization function needs to be simulated by additional degrees of freedom. For this reason, in ED we work with an Anderson impurity model (AIM), which has the following Hamiltonian form

$$H^{AIM} = \sum_m^{N_d} \epsilon_m d_m^\dagger d_m + \sum_l^{N_{bath}} \epsilon_l a_l^\dagger a_l + \sum_l (W_{lm} a_l^\dagger d_m + h.c.) + V_1 \sum_{m_1 m_2} n_{m_1} n_{m_2} . \tag{15}$$

$d_m^\dagger(d_m)$ is the creation (annihilation) operator of the impurity electron, and $N_d = 4$. V_1 is the Coulomb interaction between neighboring sites. ϵ_m is the impurity energy level. ϵ_l and W_{lm} are additional parameters introduced to simulate the hybridization function. They are often called bath degrees of freedom. In our calculation, we take $N_{bath} = 8$ and a shared-bath topology.

$$[G^{imp,-1}(i\omega_n) + \Sigma(i\omega_n)] = [i\omega_n + \mu - E_{loc} - \sum_l \frac{W^*_{m_1 l} W_{l m_2}}{i\omega_n - \epsilon_l}] , \tag{16}$$

where E_{loc} is the impurity energy level and corresponds to the local part of Eq. (1). We use χ^2-minimization to fit the left side of the above equation by choosing appropriate W_{lm} and ϵ_l. The quality of the DMFT solution, therefore, depends on the quality of fitting. In our calculations, we always carefully check the fitting parameters and, most of the time, we use the converged fitting values of $\{W, \epsilon\}$ at the neighboring parameters $a/\lambda, b/\lambda, V_1/\lambda, V_2/\lambda$ as initial values. For the DMFT calculations, we directly

used the lapack routine to diagonalize the Anderson impurity Hamiltonian. While, for the six-site CDMFT equations, we used the Lanczos algorithm [5] and also includes the nest nearest-neighbor interaction V_2.

We briefly summarize the advantages and limitations of our DMFT calculation. Understanding the condition of applicability is essential for interpreting the results and summarizing the general conclusions independent of any specific method. (1). Compared to the static mean-field theory presented in the previous section, DMFT contains dynamic fluctuations which will influence both the QAH and the CDW states. (2). The local approximation of DMFT allows only local charge fluctuations to be considered. (3). ED only works with Hamiltonian form, such that we have to use additional bath degrees of freedom to simulate the hybridization function. Limited by the memory size, one cannot take as many bath sites as wanted. In our calculations, we take $N_{bath} = 8$, which we found sufficient to fit the hybridization function with good accuracy. (4). A better treatment of non-local Coulomb interaction requires an extended-DMFT calculation, in which interactions become dynamical. Here, we simply truncate the interaction beyond the impurity size, which results in a simplification. From such approximation, we underestimate the effect of V_1 and V_2. Thus, the results we obtained provide an upper bound of the phase boundary between QAH and CDW.

[1] Q. Sui, J. Zhang, S. Jin, Y. Xia, and G. Li, Chinese Physics Letters **37**, 097301 (2020).
[2] F. D. M. Haldane, Phys. Rev. Lett. **61**, 2015 (1988).
[3] C. L. Kane and E. J. Mele, Phys. Rev. Lett. **95**, 146802 (2005).
[4] T. Fukui, Y. Hatsugai, and H. Suzuki, Journal of the Physical Society of Japan **74**, 1674 (2005).
[5] C. Lanczos, J. Res. Natl. Bur. Stand. B **45**, 255 (1950).